




Fermi level tuning and band alignment in Mn-doped InAs/GaSb

L. Riney ¹, J. Bermejo-Ortiz,² G. Krizman ³, S.-K. Bac,¹ J. Wang ¹, M. Zhukovskiy,⁴ T. Orlova,⁴
L. A. de Vaulchier,² Y. Guldner,² R. Winkler,⁵ J. K. Furdyna,¹ X. Liu,¹ and B. A. Assaf¹

¹*Department of Physics, University of Notre Dame, Notre Dame, Indiana 46556, USA*

²*Laboratoire de Physique de l'Ecole Normale Supérieure, ENS, Université PSL, CNRS, Sorbonne Université, 24 rue Lhomond, 75005 Paris, France*

³*Institut für Halbleiter- und Festkörperphysik, Johannes Kepler Universität, Linz, Altenberger Strasse 69, 4040 Linz, Austria*

⁴*Notre Dame Integrated Imaging Facility, University of Notre Dame, Notre Dame, Indiana 46556, USA*

⁵*Department of Physics, Northern Illinois University, DeKalb, Illinois 60115, USA*



(Received 29 November 2021; accepted 24 February 2022; published 10 March 2022)

InAs/GaSb hosts a broken-gap band alignment that has been shown to generate helical topological edge states. Upon the introduction of Mn into the structure, it has been predicted to host a quantized anomalous Hall effect. Here, we show that dilute Mn doping on InAs in InAs/GaSb allows a tuning of the Fermi level, the introduction of paramagnetism, but also has a nontrivial impact on the band alignment of the system. The measurement of Shubnikov–de Haas oscillations, cyclotron resonance, and a nonlinear Hall effect in Mn-doped samples indicate the coexistence of a high mobility two-dimensional electron gas and a hole gas. Conversely, in undoped InAs/GaSb, pure-*n*-type transport is observed. We hypothesize that Mn acceptor levels can pin the Fermi energy near the valence band edge of InAs, far from the interface, which introduces a strong band bending to preserve the band offset at the InAs/GaSb interface. The realization of the quantized anomalous Hall effect in this structure will thus require careful control of the band alignment to preserve topological insulating character.

DOI: [10.1103/PhysRevB.105.125301](https://doi.org/10.1103/PhysRevB.105.125301)

I. INTRODUCTION

The InAs/GaSb broken-gap III-V heterojunctions [1] can host a two-dimensional quantum spin Hall state resulting from a band-inverted electronic structure [2–5]. At the interface between the two materials, the InAs conduction subband edge lies below the GaSb valence subband edge for a given thickness range [6]. The two energy bands can hybridize and open a gap [7–9]. Thus, this interface can host two-dimensional electron states *HH1* and *E1* that have a topological band-inverted gap [2]. Various experiments have reported evidence of this band inversion or of edge states in this structure [10–13]. Magnetic exchange induced onto the energy states of this system can have exciting consequences that have not been investigated. Specifically, it was predicted to yield a quantized anomalous Hall effect (QAHE) by inducing a Zeeman splitting that restores trivial band order for one spin but maintains the inversion for the other [14]. This state has yet to be observed but can only be reached if the Fermi level lies between *HH1* and *E1* and the system has a finite magnetization. In a sample that satisfies these conditions and maintains a bulk insulating character, it is expected that chiral edge states appear without the need for Landau quantization [15].

A realistic mapping of the topological phase diagram of InAs/GaSb with magnetism introduced by the presence of Mn also requires one to preserve Landau quantization. This is needed primarily to allow a reliable determination of the strength of magnetic exchange coupling compared to the inverted gap between *HH1* and *E1* using various Landau

level spectroscopies [16,17]. It is thus important to properly quantify the extent to which Mn alters the diffusive and quantum properties of the interfacial two-dimensional electron gas (2DEG) of InAs/GaSb.

While $\text{In}_{1-x}\text{Mn}_x\text{As}$ compounds have been extensively studied in the past, those studies were limited to quantum wells, epilayers, and heterojunctions with high Mn content. Digital doping of InAs with Mn was also studied [18]. The introduction of a high concentration of Mn (> 1%) into InAs/GaSb was studied to enhance magnetism and the anomalous Hall effect in the past; however, the impact of Mn doping on quantum transport and on the band alignment in InAs/GaSb was never considered [19,18]. Given that Mn plays a doubly important role of introducing magnetism and acceptor levels in III-V materials, it is expected to have a nontrivial impact on the system. In bulk InAs, Mn impurity levels are known to occur near the valence band edge, leading to *p*-type conduction, with low mobility [19,20]. However, their behavior is yet not investigated in InAs/GaSb when introduced at dilute levels.

Here, we study the electrical and magnetic properties of paramagnetic $\text{In}_{1-x}\text{Mn}_x\text{As/GaSb}$ at low *x* (< 0.1%) grown by molecular beam epitaxy. We consider the impact of Mn on the Fermi energy and band alignment of the system. Quantum oscillations are measured up to magnetic fields reaching 16 T. We observe persistent quantum oscillations from the interfacial 2DEG of InAs/GaSb coexisting with *p*-type conduction and paramagnetism in the presence of Mn. The frequency of the oscillations and the total charge density of the 2DEG decrease with increasing Mn content. However, a hole gas starts

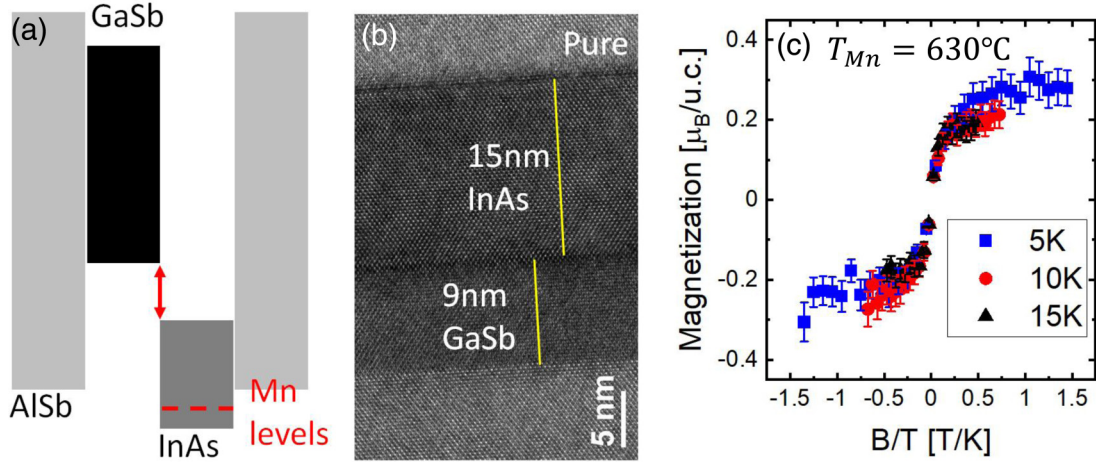


FIG. 1. (a) Band alignment diagram of InAs/GaSb bilayers grown between AlSb barriers. The position of the Mn levels is hypothetical. (b) Transmission electron microscopy images of a pure bilayer showing the thickness of each layer. (c) Magnetization versus B/T at 5, 10, and 15 K with magnetic field applied along the growth axis for sample 630. The error bars are based on the statistical standard deviation at saturation. These curves allow one to determine the Mn content of sample 630.

to emerge as Mn content or temperature is increased, without altering the qualitative behavior of the interfacial 2DEG. We thus conclude that Mn introduces a significant band bending into the system which indicates that a band structure calculation that is self-consistent with the electrostatics of the system is required to fully understand the properties of $\text{In}_{1-x}\text{Mn}_x\text{As}/\text{GaSb}$. The realization of the QAHE in this system could rest on the proper understanding and control of the band alignment.

II. RESULTS

A. Growth and characterization

$\text{In}_{1-x}\text{Mn}_x\text{As}/\text{GaSb}$ wells are grown by molecular beam epitaxy on GaAs(100). After substrates are prepared, a series of strain-relieving buffer layers is grown as follows: 250 nm AlSb, 500 nm (Al,Ga)Sb, and 22 nm AlSb as a barrier. This is followed by the GaSb well, the InAs well, a 22 nm AlSb top barrier, 95 nm (Al,Ga)Sb, and a 2–3 nm GaSb capping layer to prevent the oxidation of Al containing layers. Mn is incorporated by codeposition during the InAs growth. The structure is sketched in Fig. 1(a) in the vicinity of the wells. Throughout this paper, the nominal Mn content is denoted by the Mn cell temperature. It is also used for sample identification. The sample properties are summarized in Table I.

Figure 1(b) shows a high-resolution transmission electron microscopy (TEM) image of the InAs/GaSb interface of the pure sample. The abrupt nature of the interface is evident in the TEM images. Those images also yield a precise thickness of 15 nm for InAs and 9 nm for GaSb. In Table I, we list four samples that we study. Each sample will be referred to by the Mn cell temperature that was utilized during the growth.

Superconducting quantum interference device (SQUID) magnetometry measurements were carried out on a multiquantum well with ten periods grown under the same conditions as sample 630. The ten periods are required to enhance the paramagnetic signal. Figure 1(c) shows the magnetization plotted versus B/T for this sample, at 5, 10, and 15 K. A clear s-shaped curve is recovered, characteristic of the paramagnetism. The magnetization saturates close to $(0.26 \pm 0.04)\mu_B/\text{u.c.}$ This yields the Mn content shown in Table I for sample 630. For a lower Mn cell temperature, the paramagnetism due to Mn atoms remained below our detection capabilities. However, as will be seen later, the presence of Mn is confirmed by the changing charge density of the system.

Magnetotransport measurements are carried out at 1.5 K in a standard Oxford Instruments cryostat equipped with a superconducting magnet that can reach 16 T. Rectangular samples are cleaved from large wafers and bonded using In solder to

TABLE I. Mn cell temperature also used as sample ID, sheet resistance, Hall effect slope R_H , the carrier density extracted from Hall and Shubnikov–de Haas (SdH) oscillations, and the Mn content extracted from magnetometry where possible. For samples 600 and 615, the order of magnitude of x is estimated from the carrier density.

Mn cell (°C)	Sheet resistance (Ω)	Low field Hall slope (Ω/T)	Hall carrier density (cm^{-2})	SdH carrier density (cm^{-2})	Mn content x
0	267	−93	-6.7×10^{12}	-6.7×10^{12}	0
600	48	−88	-7.1×10^{12}	-6.5×10^{12}	$< 10^{-4}$
615	120	−73	Two-carrier types	-4.9×10^{12}	$> 10^{-4}$
630	196	−63	Two-carrier types	-3.0×10^{12}	$^a 0.0013 \pm 0.0002$

^aThe order of magnitude of x for 630 is measured using SQUID magnetometry on a multiquantum well of ten periods of AlSb/InAs/GaSb grown under the same conditions as the double wells studied here.

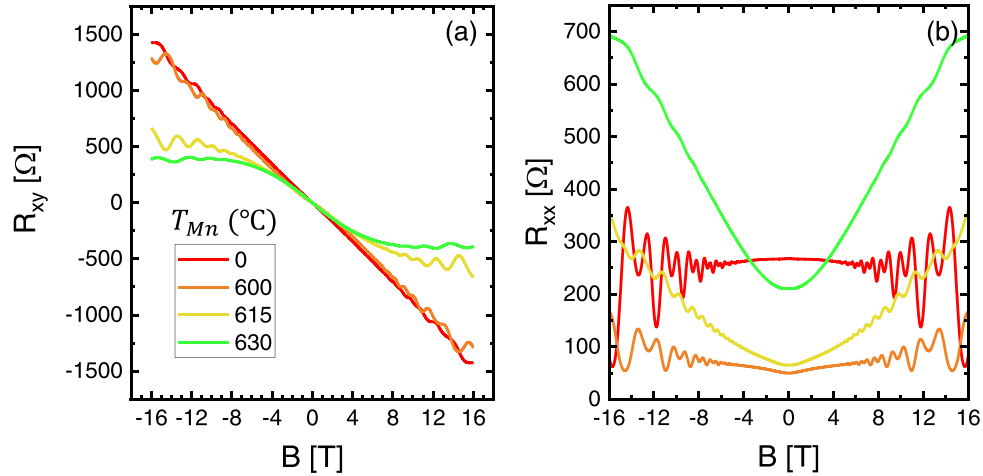


FIG. 2. (a) Hall effect and (b) magnetoresistance measured in all four samples at 1.5 K for various Mn cell temperatures.

obtain five contacts. Magneto-optical infrared spectroscopy measurements are carried out at 4.2 K up to 15 T using a cryostat system coupled with a Bruker Vertex 80v spectrometer configured for the far-infrared range. A bolometer cooled down to 4.2 K in the same bath as the sample is used to detect optical transmission T through the sample. The relative transmission $T(B)/T(B=0)$ is reported as a function of the field.

B. Quantum oscillations at various Mn contents

Figure 2 shows the variation of the Hall effect measured in the four samples grown at varying Mn cell temperatures, including an undoped sample. All exhibit an n -type Hall effect at low field and host strong quantum oscillations from Landau quantization. In Fig. 2(b), we plot the magnetoresistance measured at 1.5 K for the four samples. These initial measurements allow us to extract the diffusive transport properties of the samples that exhibit a quasilinear Hall effect. They are listed in Table I. A reduction of the Hall effect slope

at low magnetic field correlates with an increasing Mn cell temperature at which the samples were grown. The amplitude of the quantum oscillations shown in Fig. 2(b) also drops with increasing Mn content, but the magnetoresistance becomes stronger reaching 350% at 16 T for sample 630. The origin of this magnetoresistance is beyond the scope of this work, but we highlight that can be due to various mechanisms, including a two-carrier contribution from the Drude model [21], disorder effects [22], and effects related to Landau levels [23].

Figure 3(a) shows the oscillating resistance after a background is removed. A Fourier transform of the curves is performed and is shown in Fig. 3(b). It allows us to extract the oscillation frequencies as well as the n -type carrier density of the samples. We initially focus on the undoped sample, for which we obtain two frequencies that yield $n_1 = 4.2 \times 10^{12} \text{ cm}^{-2}$ and $n_2 = 2.3 \times 10^{12} \text{ cm}^{-2}$. Their sum agrees with what we extract from the Hall effect slope shown in Fig. 2, $n_H = 6.7 \times 10^{12} \text{ cm}^{-2}$. We can further understand the origin of this by carrying out self-consistent calculations in

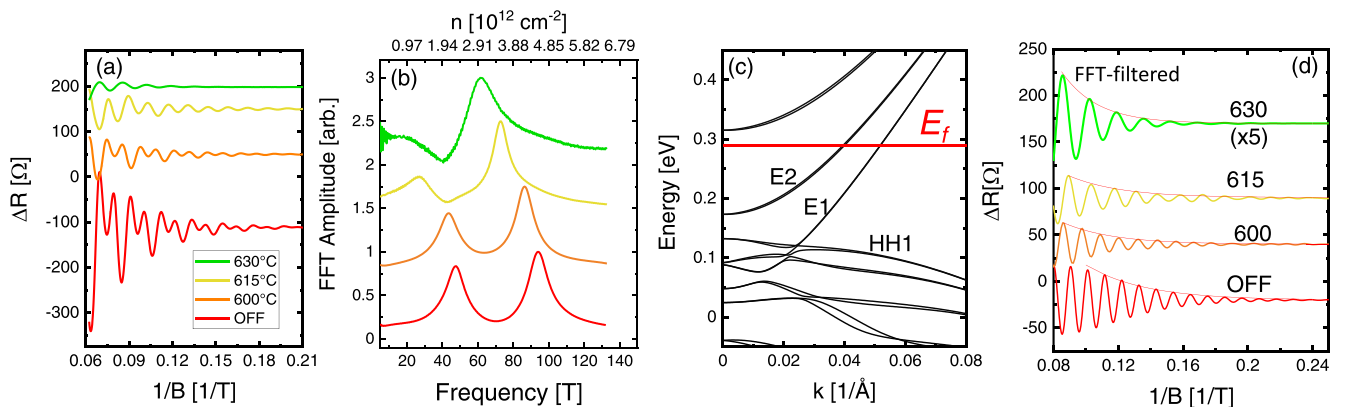


FIG. 3. (a) Shubnikov–de Haas oscillations measured in four samples labeled by the Mn cell temperature during their growth, after a background is removed. (b) FFT power spectra of the oscillations shown in (a). The spectra are normalized by the largest peak amplitude. The curves in both (a) and (b) are shifted for clarity. (c) Energy band diagram of the InAs/GaSb system calculated assuming a quasi-flat-band configuration. Zero energy corresponds to the InAs conduction band edge. The red solid line is the Fermi level E_f . E_i : i th electron subband; HH_i : i th heavy hole subband (d) FFT-filtered oscillations for the four samples.

TABLE II. Shubnikov–de Haas carrier density and mobility. The mobility μ is obtained from the decay envelope of the resistance versus $1/B$.

Mn cell (°C)	SdH carrier density (cm^{-2})	Mobility ($\text{cm}^2/\text{V s}$)
0	-6.7×10^{12}	1030 ± 60
600	-6.5×10^{12}	970 ± 60
615	-4.9×10^{12}	1000 ± 60
630	-3.0×10^{12}	690 ± 60

the Hartree approximation using an envelope function model based on the 8×8 Kane Hamiltonian [24–26]. We have assumed that homogeneously distributed bulk impurities in the InAs well compensate the n -type charge density observed in the undoped sample. The latter is peaked in the center of the well. To a good approximation, this is satisfactory inside the well and yields results consistent with the experiment. This assumption also yields flat bands in the InAs and GaSb layers as shown in Fig. 5(c). We thus model the InAs/GaSb system by taking into account the established band offset between the two materials, $E_{V,\text{GaSb}} - E_{C,\text{InAs}} = 0.15 \text{ eV}$ [27]. The elevated position of the Fermi level above the conduction band edges and our assumptions about the charge distribution being due to bulk impurities in the InAs well are confirmed by Hall measurements carried out on a control epilayer.

The model yields the weakly spin-split energy band diagram shown in Fig. 3(c), where we have marked the position of the Fermi level that agrees with the experimentally determined charge densities for the undoped sample. Indeed, the Fermi level crosses two electronlike bands, yielding Fermi wave vectors that reproduce the densities measured from quantum oscillations (calculated subband densities $n_1 = 4.3 \times 10^{12} \text{ cm}^{-2}$ and $n_2 = 2.5 \times 10^{12} \text{ cm}^{-2}$). A theoretical model that assumes flat-band conditions thus reproduces the findings of the experiments at 1.5 K, in the absence of Mn.

A small reduction of the Shubnikov–de Haas frequency and thus of the n -type doping is observed with increasing Mn content. This is consistent with the calculated band structure shown in Fig. 3(c), if one simply assumes a reduction of the Fermi level position with increasing Mn content. E_f drops from 290 meV for the pure sample, close to 220 meV for sample 630. For that sample, the charge density is found to be $n = 3.0 \times 10^{12} \text{ cm}^{-2}$. This reduction is also consistent with the established knowledge that Mn introduces acceptor levels into III-V semiconductors [28], and with previously reported p -type conduction in InAs/GaSb at high Mn content. At dilute levels, Mn acceptor states will hence compensate the native n doping of InAs.

An analysis of the Shubnikov–de Haas amplitude versus inverse magnetic field allows us to extract the mobility. We choose to focus on the higher frequency corresponding to E_1 , since the magnitude of its quantum oscillations signal is larger and yields more oscillations. We apply a bandpass filter to the fast Fourier transform (FFT) data shown in Fig. 3(b) to isolate the high frequency signal. This isolated signal is plotted versus $1/B$ in Fig. 3(d) for the four samples. Only the lowest temperature data is treated. The envelope of the decaying oscillations is then fit to a Dingle exponential expressed as

$$\frac{\Delta R(1/B)}{\Delta R(0)} = \exp\left(-\frac{\pi}{\mu B}\right).$$

The resulting mobilities μ are shown in Table II.

C. Cyclotron resonance at various Mn contents

To further corroborate this picture, cyclotron resonance measurements are carried out at 4.2 K in the far infrared. The optical transmission in the far infrared for various fields measured for three samples (600, 615, and 630) is shown in Fig. 4(a). A minimum that shifts to higher energy versus magnetic field is observed indicating that the minimum is related to Landau levels. The position of the minimum is consistent with what is expected for the cyclotron resonance

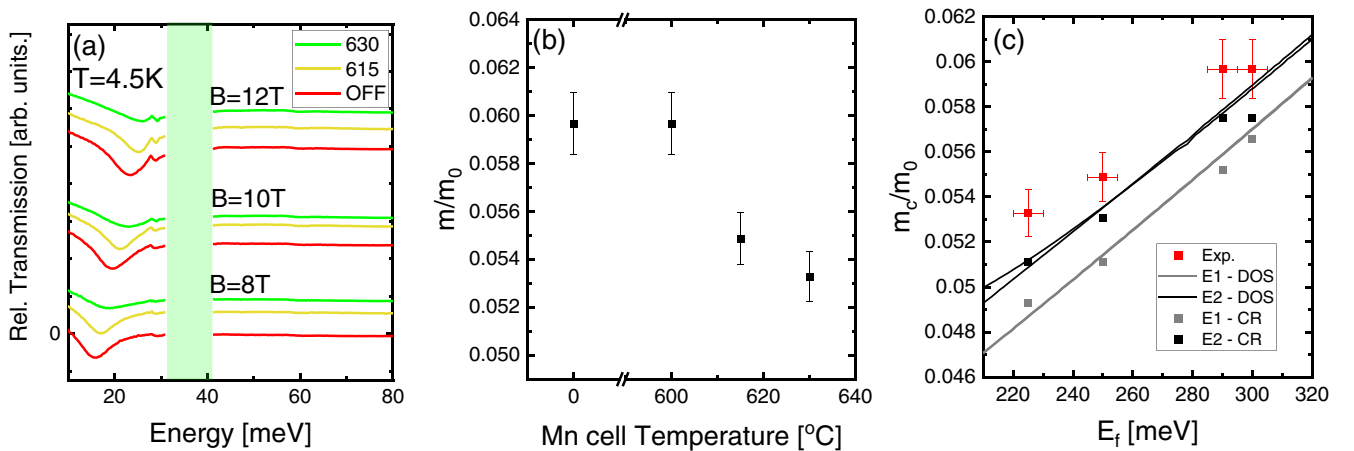


FIG. 4. Cyclotron resonance (CR) measurements in the far infrared at different magnetic fields, at 4.2 K. The green box represents the reststrahlen band of the GaAs substrate. (b) Cyclotron masses extracted for the four samples from the cyclotron resonance at 12 T. (c) Variation of m_c/m_0 versus the Fermi energy. The experimental values are shown in red. The values recovered from the computed CR using the model are shown as gray and black dots for E_1 and E_2 , respectively (see Appendix A). The gray and black solid lines represent the variation of the density of states effective mass for E_1 and E_2 , respectively.

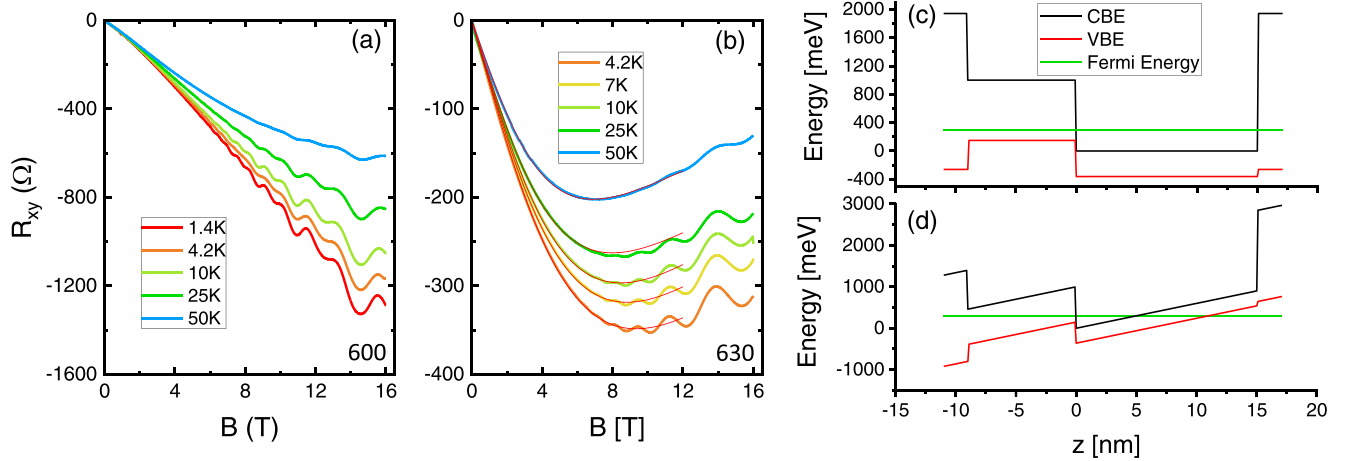


FIG. 5. Hall effect versus increasing temperature in samples 600 (a) and 630 (b). (c) Band alignment of InAs/GaSb without Mn. The position of the Fermi level is fixed to be consistent with our quantum oscillations data. (d) Hypothetical sketch of the band alignment for Mn-doped InAs/GaSb. The Fermi energy has to cross the valence band away from the InAs/GaSb interface, but the band offset has to be respected at the interface. CBE: conduction band edge; VBE: valence band edge.

of the 2DEG for high Landau indices. The cyclotron mass extracted from this data at 12 T is shown for various Mn contents in Fig. 4(b). The resonance yields an effective mass close to $0.0595 m_0$ for samples 0 and 600, consistent with what is expected when $E_f = 300\text{--}290\text{ meV}$. This value, $0.0595 m_0$, is higher than what was previously reported [16,9], simply because the position of the Fermi energy is higher above the conduction band edges. At the same time, the energy of the transmission minimum increases with increasing Mn content, indicating that the cyclotron mass is decreasing. We avoid comparing the cyclotron mass to the mass that one can extract from the temperature dependence of quantum oscillations since we found it nontrivial to reliably deconvolute the signal containing two oscillation frequencies, at all temperatures. This problem has been considered for two-dimensional hole gases in the past [29].

These measurements confirm that the quantum oscillations are due to the interfacial 2DEG of InAs/GaSb with the Fermi level crossing electron subbands of comparable effective mass. As more Mn is introduced, the cyclotron mass decreases, consistent with a slight lowering of the Fermi level deduced from Shubnikov–de Haas measurements. One expects the effective mass to depend on energy in this system, since the bands are highly nonparabolic away from the band edges. The Fermi energy can be extracted by matching the measured Fermi wave vector from the higher Shubnikov–de Haas frequency to the subband structure shown in Fig. 3(c). The Landau fan chart corresponding to the band diagram shown in that figure is shown in Appendix A. It is used to extract the cyclotron energy expected for E1 and E2 at 12 T at each density. This is then used to extract the cyclotron mass from the model. This calculated mass is also plotted versus Fermi energy in Fig. 4(c). The measured and calculated cyclotron mass for E2 agree within two standard deviations, but qualitatively, the decreasing trend of m_c/m_0 that is obtained from the experiment is well reproduced by the model. We avoid using the temperature dependence of the quantum oscillations to extract the cyclotron mass, as it is nontrivial to

carry out this procedure when two oscillation series coexist in a 2DEG system. This issue has been discussed in the past for GaAs-based 2DEG [29], but it is worth revisiting in a separate work for InAs/GaSb.

From these measurements, it is thus evident that a 2DEG yields quantum oscillations in $\text{In}_{1-x}\text{Mn}_x\text{As}$, in the presence of paramagnetism. Its charge density and the effective mass drop as more Mn is introduced into the system.

D. Coexistence of electrons and holes in Mn-doped InAs/GaSb

The Hall effect measured up to 16 T shown in Figs. 2 and 5 is inconsistent with that picture when Mn is introduced. Without Mn, InAs is lightly n type but E_f is well above the valence band edge $HH1$ of GaSb as shown in Fig. 3(c) and n_H agrees with the total n extract from quantum oscillations. The Hall voltage becomes nonlinear and its slope changes sign when the Mn content is increased as seen in Figs. 5(a), 5(b), and Fig. 2. This indicates the presence of a finite density of holes in the system. In two samples, 600 and 630, quantum oscillations persist up to 50 K as shown in Figs. 5(a) and 5(b). In sample 600, the Hall effect has a negative slope at 1.5 K, but slowly develops a nonlinearity with increasing temperature [Fig. 5(a)]. In sample 630, the Hall effect is nonlinear at 1.5 K. Its slope is always negative at low field, but a positive slope develops at high field and gets enhanced with increasing temperature [Fig. 5(b)]. The nonlinearity of the Hall effect upon the introduction of Mn indicates the presence of a p -type conduction channel. We carry out a more quantitative analysis of the nonlinear Hall effect in Appendix B. We note here that the nonlinearity of the Hall effect is unlikely to be caused by the anomalous Hall effect. This is because as temperature increases, the nonlinearity is enhanced, contrary to what is expected to happen for an anomalous Hall effect resulting from magnetism.

At the Fermi energies extracted for the interfacial 2DEG, we do not expect E_f to cross the valence subbands of GaSb in our model that assumes flat-band conditions [Fig. 5(c)]. Let us consider the case of sample 630 with the highest Mn

concentration. The quantum oscillations observed in that sample yield a Fermi wave vector consistent with what is obtained from the calculation [Fig. 3(c)] that assumed the known band alignment of InAs/GaSb [Fig. 5(c)], for $E_f = 220$ meV. However, the observation of a hole gas in the Hall effect is not consistent with these results. E_f remains too high to yield any crossing with the GaSb valence subbands at 220 meV. This fact leads us to conclude that the flat-band assumption used for undoped InAs/GaSb no longer holds when Mn is introduced. At high Mn content, InAs likely becomes p type far away from the interface as Mn yields impurity levels near its valence band edge [20,30]. The Fermi level should thus lie near the valence band edge of InAs away from its interface with GaSb. A substantial band bending effect could result from this, to preserve the band offset at the interface with GaSb as shown in Fig. 5(d). This hypothetical alignment can yield a situation that maintains the quantum oscillations resulting from the 2DEG while introducing a low mobility hole gas away from the interface, that only impacts diffusive transport such as the normal Hall effect.

III. CONCLUSION

From this study, we conclude that Mn indeed impacts the band alignment and electronic structure of InAs/GaSb, beyond simply introducing magnetic exchange and reducing the charge density. At low Mn content, $\text{In}_{1-x}\text{Mn}_x\text{As}/\text{GaSb}$ samples host a coexisting 2DEG and hole gas that is due to band bending caused by the Mn impurity levels in InAs. We note that paramagnetism was measured in sample 630, but we could not detect the effect of magnetic exchange splitting in Shubnikov–de Haas measurements since the Fermi level crosses high index Landau levels at 16 T ($n > 4$). But importantly, we have shown that Mn allows the tuning of the Fermi level and alters the band alignment in InAs/GaSb. Its action is highly nontrivial and fundamentally interesting. Its understanding requires a better knowledge of the charge distribution and the band bending profile of the system to enable reliable self-consistent calculations. The realization of a QAHE in this structure can only be achieved if the action of Mn is properly quantified and controlled, since this band bending can generate additional diffusive conduction channels that will short out the chiral edge states.

ACKNOWLEDGMENTS

This work is supported by National Science Foundation Grant No. NSF-DMR-1905277. We also acknowledge support from ANR Grant No. 19-CE30-022-01. We thank Mansour Shayegan for useful conversations.

APPENDIX A: LANDAU LEVELS

The Landau level fan chart corresponding to the band structure shown in Fig. 3(c) is shown in Fig. 6(a). Figure 3(c) allows one to determine the Fermi energy E_f corresponding to each k_f extracted from quantum oscillations for the first subband ($E1$). We use this fan chart to extract the cyclotron mass at 12 T, from the intraband transition expected to be active for each sample. The analysis is shown for sample

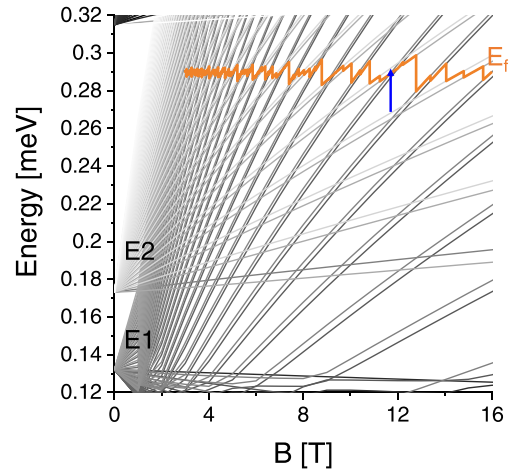


FIG. 6. (a) Landau fan chart showing the first and second subbands $E1$ and $E2$ of InAs. The Fermi energy is computed and shown for sample 600, by assuming a constant charge density. The blue arrow represents one of the allowed transitions at 12 T.

600 with $E_f = 290$ meV. The variation of E_f is computed by assuming a constant charge density. At 12 T, active intraband transitions are those between consecutive Landau levels with identical spin, i.e., $(N)^{\text{up}}$ to $(N+1)^{\text{up}}$ for which the initial state is occupied (i.e., below E_f) and final state unoccupied (above E_f). These selection rules are established for III-V quantum wells in the Faraday geometry. We consider transitions belonging to $E1$ and $E2$. The computed transition energy allows us to determine the cyclotron mass defined as

$$\frac{m_c}{m_0} = \frac{1}{m_0} \frac{\hbar e B}{E_{N+1} - E_N}.$$

The resulting effect masses are shown in Fig. 4(c).

APPENDIX B: TWO-CARRIER DRUDE ANALYSIS

The nonlinear Hall effect is analyzed using a two-carrier Drude model up to 12 T. Curve fits to the data shown in Fig. 5 are obtained using the equations

$$R_{xy} = \frac{aB + bB^3}{1 + cB^2}, \quad \rho_{xx} = \frac{\rho_0 + b'B^2}{1 + cB^2},$$

$$a = \frac{R_1 \rho_2^2 + R_2 \rho_1^2}{(\rho_1 + \rho_2)^2}, \quad b = \frac{R_1 R_2 (R_1 + R_2)}{(\rho_1 + \rho_2)^2},$$

TABLE III. Drude model fit parameters. n is fixed to $3 \times 10^{12} \text{ cm}^{-2}$, the value recovered from Shubnikov–de Haas measurements.

Temperature (K)	p (10^{14} cm^{-2})	μ_p ($\text{cm}^2/\text{V s}$)	μ_n ($\text{cm}^2/\text{V s}$)
4.2	2.4	21	2470
7	2.2	26	2450
10	2.3	25	2580
25	4.4	15	2680
50	4.1	18	2920

$$c = \frac{(R_1 + R_2)^2}{(\rho_1 + \rho_2)^2}, \quad \rho_0 = \frac{\rho_1 \rho_2}{\rho_1 + \rho_2},$$

$$b' = \frac{\rho_1 R_2^2 + \rho_2 R_1^2}{(\rho_1 + \rho_2)^2}, \quad \rho_i = \frac{1}{n_i e \mu_i}, \quad R_i = \frac{1}{n_i e}.$$

n_i and μ_i represent the charge density and mobility of each channel. We avoid carrying a fit to the magnetoresistance as other effects can cause it to change. We also restrict the analysis to sample 630 since for sample 600 the curvature of R_{xy} is weak and the reliability of the fitting parameters is compromised. Table III lists the parameters obtained from the fit.

- [1] H. Kroemer, The family (InAs, GaSb, AlSb) and its heterostructures: A selective review, *Phys. E (Amsterdam, Neth.)* **20**, 196 (2004).
- [2] I. Knez, R.-R. Du, and G. Sullivan, Evidence for Helical Edge Modes in Inverted InAs/GaSb Quantum Wells, *Phys. Rev. Lett.* **107**, 136603 (2011).
- [3] S. S. Krishtopenko and F. Teppe, Quantum spin Hall insulator with a large bandgap, Dirac fermions, and bilayer graphene analog, *Sci. Adv.* **4**, eaap7529 (2018).
- [4] C. Liu, T. L. Hughes, X.-L. Qi, K. Wang, and S.-C. Zhang, Quantum Spin Hall Effect in Inverted Type-II Semiconductors, *Phys. Rev. Lett.* **100**, 236601 (2008).
- [5] L. Du, I. Knez, G. Sullivan, and R.-R. Du, Robust Helical Edge Transport in Gated InAs/GaSb Bilayers, *Phys. Rev. Lett.* **114**, 096802 (2015).
- [6] L. L. Chang and L. Esaki, Electronic properties of InAs-GaSb superlattices, *Surf. Sci.* **98**, 70 (1980).
- [7] M. J. Yang, C. H. Yang, B. R. Bennett, and B. V. Shanabrook, Evidence of a Hybridization Gap in “Semimetallic” InAs/GaSb Systems, *Phys. Rev. Lett.* **78**, 4613 (1997).
- [8] L. Du, X. Li, W. Lou, G. Sullivan, K. Chang, J. Kono, and R.-R. Du, Evidence for a topological excitonic insulator in InAs/GaSb bilayers, *Nat. Commun.* **8**, 1971 (2017).
- [9] S. S. Krishtopenko, S. Ruffenach, F. Gonzalez-Posada, G. Boissier, M. Marcinkiewicz, M. A. Fadeev, A. M. Kadykov, V. V. Rumyantsev, S. V. Morozov, V. I. Gavrilenko, C. Consejo, W. Desrat, B. Jouault, W. Knap, E. Tournié, and F. Teppe, Temperature-dependent terahertz spectroscopy of inverted-band three-layer InAs/GaSb/InAs quantum well, *Phys. Rev. B* **97**, 245419 (2018).
- [10] F. Nichele, A. N. Pal, P. Pietsch, T. Ihn, K. Ensslin, C. Charpentier, and W. Wegscheider, Insulating State and Giant Nonlocal Response in an InAs/GaSb Quantum Well in the Quantum Hall Regime, *Phys. Rev. Lett.* **112**, 036802 (2014).
- [11] M. Karalic, S. Mueller, C. Mittag, K. Pakrouski, Q. Wu, A. A. Soluyanov, M. Troyer, T. Tschirky, W. Wegscheider, K. Ensslin, and T. Ihn, Experimental signatures of the inverted phase in InAs/GaSb coupled quantum wells, *Phys. Rev. B* **94**, 241402 (2016).
- [12] F. Couëdo, H. Irie, K. Suzuki, K. Onomitsu, and K. Muraki, Single-edge transport in an InAs/GaSb quantum Spin Hall insulator, *Phys. Rev. B* **94**, 035301 (2016).
- [13] F. Qu, A. J. A. Beukman, S. Nadj-Perge, M. Wimmer, B.-M. Nguyen, W. Yi, J. Thorp, M. Sokolich, A. A. Kiselev, M. J. Manfra, C. M. Marcus, and L. P. Kouwenhoven, Electric and Magnetic Tuning Between the Trivial and Topological Phases in InAs/GaSb Double Quantum Wells, *Phys. Rev. Lett.* **115**, 036803 (2015).
- [14] Q.-Z. Wang, X. Liu, H.-J. Zhang, N. Samarth, S.-C. Zhang, and C.-X. Liu, Quantum Anomalous Hall Effect in Magnetically Doped InAs/GaSb Quantum Wells, *Phys. Rev. Lett.* **113**, 147201 (2014).
- [15] F. D. M. Haldane, Model for a Quantum Hall Effect without Landau Levels: Condensed-Matter Realization of the “Parity Anomaly,” *Phys. Rev. Lett.* **61**, 2015 (1988).
- [16] Y. Guldner, J. P. Vieren, P. Voisin, M. Voos, J. C. Maan, L. L. Chang, and L. Esaki, Observation of double cyclotron resonance and interband transitions in InAs-GaSb multi-heterojunctions, *Solid State Commun.* **41**, 755 (1982).
- [17] S. Ruffenach, S. S. Krishtopenko, L. S. Bovkun, A. V. Ikonnikov, M. Marcinkiewicz, C. Consejo, M. Potemski, B. Piot, M. Orlita, B. R. Semyagin, M. A. Putyato, E. A. Emel’yanov, V. V. Preobrazhenskii, W. Knap, F. Gonzalez-Posada, G. Boissier, E. Tournié, F. Teppe, and V. I. Gavrilenko, Magnetoabsorption of Dirac fermions in InAs/GaSb/InAs “three-layer” gapless quantum wells, *JETP Lett.* **106**, 727 (2017).
- [18] X. Liu, W. L. Lim, L. V. Titova, T. Wojtowicz, M. Kutrowski, K. J. Yee, M. Dobrowolska, J. K. Furdyna, S. J. Potashnik, M. B. Stone, P. Schiffer, I. Vurgaftman, and J. R. Meyer, External control of the direction of magnetization in ferromagnetic InMnAs/GaSb heterostructures, *Phys. E (Amsterdam, Neth.)* **20**, 370 (2004).
- [19] H. Munekata, A. Zaslavsky, P. Fumagalli, R. J. Gambino, A. Zaslavsky, and P. Fumagalli, Preparation of (In,Mn)As/(Ga,Al)Sb magnetic semiconductor heterostructures and their ferromagnetic characteristics, *Appl. Phys. Lett.* **63**, 2929 (1993).
- [20] T. Dietl and H. Ohno, Dilute ferromagnetic semiconductors: Physics and spintronic structures, *Rev. Mod. Phys.* **86**, 187 (2014).
- [21] N. Ashcroft and N. Mermin, *Solid State Physics*, 1st ed. (Saunders College Publishing, New York, 1976).
- [22] M. M. Parish and P. B. Littlewood, Non-saturating magnetoresistance in heavily disordered semiconductors, *Nature (London)* **426**, 162 (2003).
- [23] V. Renard, Z. D. Kvon, G. M. Gusev, and J. C. Portal, Large positive magnetoresistance in a high-mobility two-dimensional electron gas: Interplay of short- and long-range disorder, *Phys. Rev. B* **70**, 033303 (2004).
- [24] R. Winkler, *Spin-Orbit Coupling Effects in Two-Dimensional Electron and Hole Systems* (Springer, Berlin, 2003).
- [25] G. Bastard, *Wave Mechanics Applied to Semiconductor Heterostructures (Les éditions de physique)* (Les Ulis, France, 1996).
- [26] G. Bastard, Superlattice band structure in the envelope-function approximation, *Phys. Rev. B* **24**, 5693 (1981).

- [27] I. Vurgaftman, J. R. Meyer, and L. R. Ram-Mohan, Band parameters for III–V compound semiconductors and their alloys, *J. Appl. Phys.* **89**, 5815 (2001).
- [28] F. Marcinowski, J. Wiebe, F. Meier, K. Hashimoto, and R. Wiesendanger, Effect of charge manipulation on scanning tunneling spectra of single Mn acceptors in InAs, *Phys. Rev. B* **77**, 115318 (2008).
- [29] B. Habib, E. Tutuc, S. Melinte, M. Shayegan, D. Wasserman, S. A. Lyon, and R. Winkler, Spin splitting in GaAs (100) two-dimensional holes, *Phys. Rev. B* **69**, 113311 (2004).
- [30] M. K. Parry and A. Krier, Liquid phase epitaxial growth and photoluminescence of Mn-doped InGaAs with InAs-enriched composition, *J. Cryst. Growth* **139**, 238 (1994).